Section 5

Development of and studies with regional and convective-scale atmospheric models and ensembles.

Effect of the initial temperature field correction on weather parameters in the short-range numerical forecast

D. Blinov[1], A. Revokatova[1,2], I. Rozinkina[1], G. Rivin[1,3]

[1])Hydrometeorological Research Center of the Russian Federation, Bolshoi Predtechensky per. 11–13, Moscow 123242, Russia
[2])Yu. A. Izrael Institute of Global Climate and Ecology, Glebovskaya 20B, Moscow 107258, Russia
[3]) Geographic Faculty, Department of Meteorology and Climatology, Lomonosov Moscow State University,
GSP-1, Leninskie Gory, Moscow 119991, Russia
*Correspondence: denisblinov@ya.ru, revokatova@gmail.com (A.R.); gdaly.rivin@mail.ru (G.R.); inna.rozinkina@mail.ru

Introduction

The purpose of this work is to test the technology of correction of initial fields of temperature of the near-surface air and upper soil levels in the COSMO-Ru7 configuration (grid spacing - 7 km, European Part of Russia and Eastern Europe) of COSMO model. This additional correction (imposed on the results of a global data assimilation system) is based on data of weather stations network (transferred in the SYNOP code).

There are several different configurations COSMO-Ru of the COSMO model in the COSMO-Ru weather forecasting system operated in the Hydrometcenter of Russia [Rivin et al., 2019]. Each configuration is characterized by its own integration domain, spatial and time steps, forecast length, etc. The examined technique is included only in the COSMO-Ru7 configuration. This work demonstrates how the correction affects the forecast of various meteorological parameters besides temperature, based on a comparison of the results of various configurations (operative runs for a full year are considered).

The correction algorithm

To perform the correction of initial fields, a specific module was developed, implemented, and tested. Based on the model initial data and 2m temperature (T2m) observations, the temperature on certain atmospheric and soil levels is refined and the updated initial data for a forecast is formed.

The general structure of the module is the following:
- Reading T2m observations at weather stations (available in the SYNOP code);
- Preparation of the first guess field T2m* at the COSMO-Ru7 grid using the initial data for starting the COSMO-Ru7 configuration;
- Interpolation of the T2m* field to the station locations;
- Calculation of increments Δt2m (observation - first guess);
- Data quality control of increments and rejection of erroneous data;
- Analysis of the increments Δt2m by a Cressman-like method, horizontal interpolation to the COSMO-Ru7 grid;
- Calculation of a refined field T2m** as a sum of T2m* and Δt2m;
- Calculation of new air temperature fields for 5 lower atmospheric levels by adding the increment Δt2m with a certain weight to the initial temperature values. The weight decays from unity at the lowest model level to zero at the sixth level from the bottom (stretching the temperature increments Δt2m to the overlying air);
- Calculation of new soil temperature fields for 5 levels below the land surface in the same manner as it was done for the atmospheric levels. The weight decays from unity at the surface soil level to zero at the sixth soil level (stretching the temperature increments Δt2m to the soil).

Methods

The impact of the 2m-temperature correction on short-range forecasts of surface air temperature, dew point temperature, wind gusts, cloudiness and precipitation is analyzed. The results were verified using the mean absolute error (MAE). The matching of stations and model grid nodes was carried out by interpolation for the nearest neighbor.

We evaluated the changes in the short- range forecast quality for winter (DJF) and summer (JJA) separately. The assessment was made for the following three domains: the Southern part of European Russia (with mountains), the Central part of European Russia (without mountains) and the entire European territory of Russia (ETR) for the forecasts started at four different times: 00, 06, 12, 18 UTC. Due to the limited size of the paper, we have to focus mostly on the results obtained for the European territory of Russia for the forecasts started at 00 UTC. In the figures below we show the results for three different model configurations: 1) COSMO-Ru7 (grid spacing - 7 km, [Rivin et al., 2015]), 2) COSMO-Ru6ENA (6.6 km, calculation domain is the entire Russia and the adjoining regions [Rivin et al., 2019]), 3) COSMO-Ru13ENA (13.2 km, the domain is the same as in COSMO-Ru6ENA) [Rivin et al., 2015]).

Results

The results based on seasonal averaging are summarized below for a set of key weather parameters:
- T2m: the positive effect of the temperature correction is more noticeable in winter than in summer (Fig.1a, b) and is observed during the entire short-range forecast.
- Td2m (dew point at 2m): As for T2m, the favorable effect is more noticeable in winter (Fig. 2a). COSMO-Ru7 with the correction module was almost always better than the other configurations primarily at the beginning of the forecast, the advantage becomes less pronounced later.
- Wind gusts: COSMO-Ru7 demonstrates better skill (smaller MAE) than the configuration COSMO-Ru6ENA characterized by the comparable resolution (7 km vs 6.6 km). The fields predicted by COSMO-Ru13ENA are smoother and this results in smaller MAE. Note that this fact does not permit us to conclude categorically that the forecasts of COSMO-Ru13ENA are better than much more detailed forecasts of COSMO-Ru7 and COSMO-Ru6ENA. Verification of highly variable fields like wind gusts cannot be based on MAE only, categorical and spatial scores should complement them. These scores will be considered in future research.

- Total Cloudiness: The effect was observed for the total cloudiness averaged within a 30-km radius around weather stations. Generally the cloudiness is better predicted with COSMO-Ru7 than with COSMO-Ru6ENA and COSMO-Ru13ENA (Fig. 3 *a, b*). The positive effect of the correction is evident during the whole forecast in the cold period (Fig. 3*a*). In summer, COSMO-Ru7 obviously wins only at the beginning of the forecast, later the resolution plays more important role and COSMO-Ru13ENA became the worst (Fig. 3b).
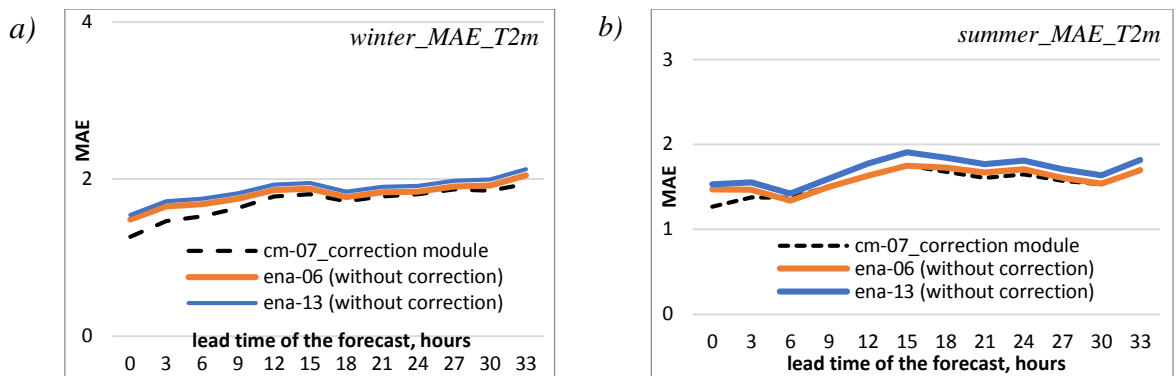

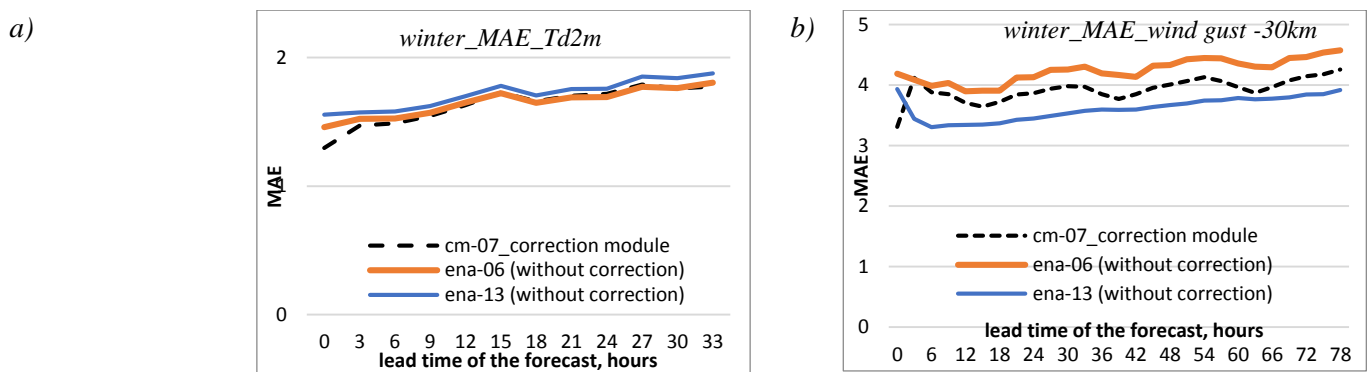Figure 1. MAE for temperature at 2 meters(° C): a) winter (DJF) and b) summer (JJA)

Figure 2. MAE for: a) dew point temperature at 2 meters(° C), b) wind gust at 10 meters (maximum in the 30-km radious m/s).
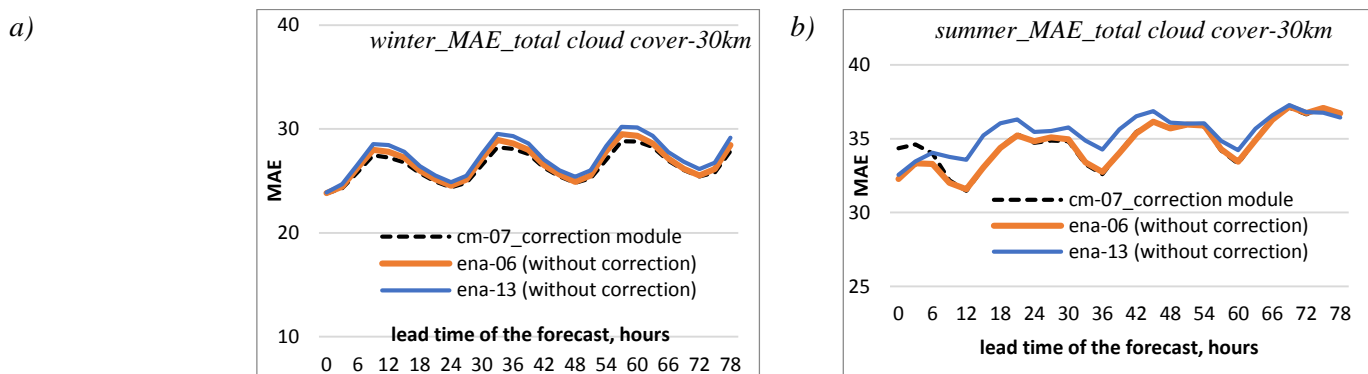

Figure 3. MAE for total cloud cover (mean in 30-km radious, %): a) winter (DJF);b) summer (JJA).

For two other domains considered in the study the results were mostly close to those presented above. However, in the southern regions of Russia COSMO-Ru7 & COSMO-Ru6ENA showed larger deviations wrt to COSMO-Ru13 ENA at the begining of the forecasts caused by the difference in resolution.

Our results show that the correction of temperature on the near-surface atmospheric model levels and on the upper soil levels based on T2m temperature measurements has positive influence to the forecasts of T2m, Td2m, cloudiness and wind gusts. The effect is uncertain for forecasts of other parameters. Probably, it can be found in some specific cases, but this was out of the scope of the present study.

References

Rivin G.S., Rozinkina I.A., Vil'fand R.M. et al. The COSMO-Ru system of nonhydrostatic mesoscale short-range weather forecasting of the Hydrometcenter of Russia: The second stage of implementation and development. Russian Meteorology and Hydrology. 2015. T. 40. № 6. C. 400-410.

Rivin G.S., Rozinkina I.A, Astakhova E.D et al. COSMO-Ru high-resolution short-range numerical weather prediction system: its development and applications. Hydrometeorological Investigations and forecasts. 2019, № 4.-374. pp. 37-53.

Numerical simulation of the melting layer with a distorted bright band, observed on February 15, 2014, in Japan

Akihiro Hashimoto[1], Sento Nakai[2], Masaki Katusmata[3] and Syugo Hayashi[1]

1) Meteorological Research Institute, Japan Meteorological Agency, Tsukuba, Japan

2) Snow and Ice Research Center, National Research Institute for Earth Science and Disaster Resilience, Nagaoka, Japan

3) Japan Agency for Marine-Earth Science and Technology, Yokosuka, Japan

1. Introduction

A melting layer is typically identified as a narrow horizontal layer showing a strong radar reflectivity factor, namely a bright band, just below freezing level in range–height indicator (RHI). The same melting layer is observed as a circular bright band in a plan position indicator (PPI). The shape of a bright band in PPI is sometimes distorted by some factors such as sloping melting layer and/or nonuniform spatial distributions of hydrometeor and so on (Boodoo et al, 2010; Katsumata et al., 2016; Shusse et al. 2019). Therefore, monitoring a bright band on PPI can provide information about the characteristics of a melting layer in a wide area. On the other hand, since the observed shape of a bright band is a result of integrated effects from various processes such as dynamical, thermodynamical, and microphysical processes, it is necessary to use not only radar observation but also other observations and numerical simulations for understanding connections between physical processes in melting layer and observed bright band.

In the early morning of 15 February 2014, a circular bright band was observed over the Kanto Plain of Japan for several hours. In the beginning, the bright band showed a distorted shape, and then, changed its shape to a circle in a couple of hours. This report gives the preliminary results on the factor affecting the shape of the bright band and its transition in PPI, based on a numerical simulation.

2. Numerical simulations

A numerical simulation system was established based on the Japan Meteorological Agency's nonhydrostatic model (JMA-NHM, Saito *et al.*, 2006) using the option of a double-moment bulk cloud microphysics scheme to predict both the mixing ratio and concentration of particles for all hydrometeor classes (i.e., cloud water, rain, cloud ice, snow, and graupel).

Numerical simulations were first performed at a horizontal resolution of 5 km (5km-NHM) over a 2500 km × 2500 km wide domain as shown in Fig. 1. Following this, the simulation with a 1-km horizontal resolution was performed (1km-NHM).

In the 5km-NHM simulation, the top height of the model domain was 22.1 km. The vertical grid spacing ranged from 40 m at the surface to 723 m at the top of the domain. Sixty vertical layers in a terrain-following coordinate system were employed. The integration time was 45 hours, with a time-step of 15 s. The initial and boundary conditions were obtained from the JMA's mesoscale analysis data (MANAL). The initial time was set to 1500 JST (UTC + 9) on 13 February 2014. Boundary conditions were provided with steps every 3 hours.

Corresponding author: Akihiro Hashimoto, Meteorological Research Institute, 1-1 Nagamine, Tsukuba, 305-0052, Japan. E-mail: ahashimo@mri-jma.go.jp
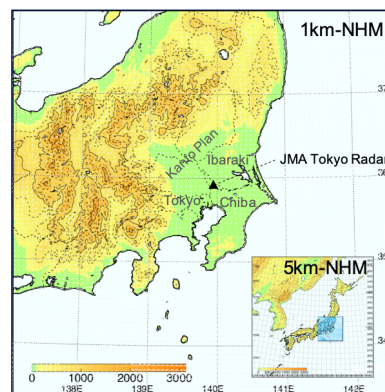
Fig. 1. Computational domains for the numerical simulations: 5km- and 1km-NHM.

The vertical grid arrangement in the 1km-NHM was the same as in the 5km-NHM, and the domain size was 500 km × 500 km (Fig. 1). The integration time used was 30 hours with a time step of 4 s. The initial and boundary conditions were obtained from the 5km-NHM simulation. The initial time for the 1km-NHM simulation was 6 hours later than that of the 5km-NHM.

3. Observed bright band

Figure 2 shows the imageries of radar/raingauge analyzed precipitation intensity during the early morning on 15 February 2014 provided by JMA. Since these imageries are made by including radar reflectivity factor in PPI scans at different elevation angles, bright band features appear in the imageries when a melting layer exists. At 0030 JST, apparently strong precipitation up to several tens mm h^{-1} was detected over a part of Tokyo, Chiba, and Ibaraki prefectures, while most of Kanto Plain and surrounding area were widely covered by weak precipitation. This apparently strong precipitation area looked firstly D-shape (Fig. 2a), then gradually changed its shape, and finally became almost a circle (Fig. 2c), a typical feature of a bright band.

4. Results of numerical simulation

Figure 3 shows the simulated snow and graupel amount below the freezing level (melting snow and graupel) which is plotted as the 3.8º PPI centered at the JMA Tokyo radar located in Kashiwa city, simply representing the spatial distribution of a bright band in the model. The D-shape appeared at 0100 JST (Fig.3a). It gradually changed and finally became a circle (Fig. 3c). This simulated feature is essentially consistent with that observed (Fig.2). Figure 4 shows the vertical distribution of the mixing ratio of melting snow and graupel particles, exactly representing
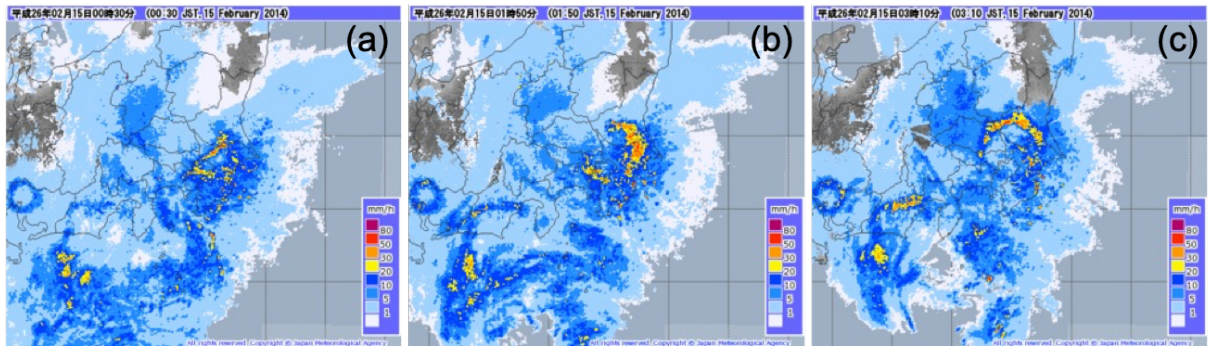
Fig. 2. Imageries of radar/raingauge analyzed precipitation intensity at (a) 0030, (b) 0150, and (c) 0310 JST on 15 February 2014 provided by JMA.
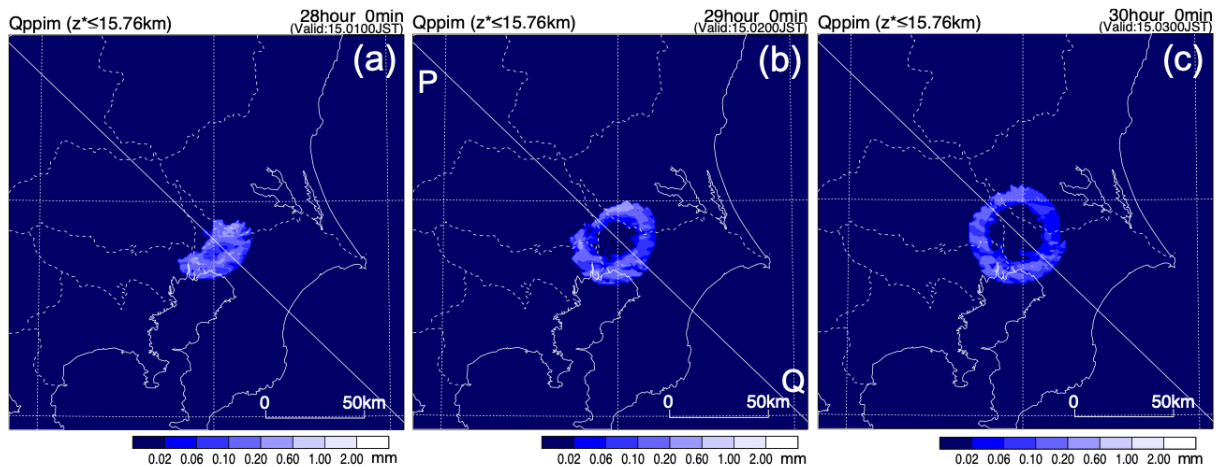

Fig. 3. Simulated PPI of snow and graupel amount below the freezing level at (a) 0100, (b) 0200, and (c) 0300 JST on 15 February 2014.

the melting layer in the model. While, on the southeast side, the melting layer was located at about 1.3 km height, it fell to the ground around the half of line PQ. This system moved to the northwest. On the ground, simulated air temperature declined from the southeast to northwest across the freezing point, which was well consistent with the surface observation (not shown). The results of numerical simulation indicated that the observed D-shape bright band and its transition to a circle were caused by the steeply sloping melting layer moving from the southeast to the northwest.

Acknowledgment

References

Boodoo, S., D. Hudak, N. Donaldson, and M. Leduc, 2010: Application of dual-polarization radar melting-layer detection algorithm. *J. Apple. Met. Clim.*, 49, 1779-1793.

Katsumata, M., S. Mori, B. Geng, and J. Inoue, 2016: Internal structure of ex-Typhoon Phanfone (2014) under an extratropical transition as observed by the research vessel Mirai, *Geophys. Res. Lett.*, 43, 9333–9341, doi:10.1002/2016GL070384.

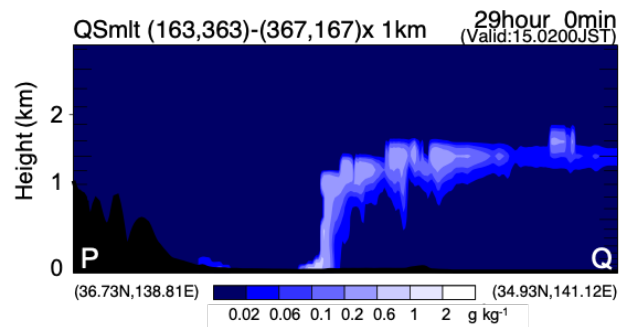Saito, K., T. Fujita, Y. Yamada, J. Ishida, Y. Kumagai, K.

Fig. 4. Simulated distribution of mixing ratio of snow and graupel particles below freezing level in the vertical cross-section on the line P-Q shown in Fig.3b at 0200 JST on 15 February 2014.

Aranami, S. Ohmori, R. Nagasawa, S. Kumagai, C. Muroi, T. Kato, H. Eito, and Y. Yamazaki, 2006: The operational JMA nonhydrostatic mesoscale model. *Mon. Wea. Rev.*, **134**, 1266–1298.

Shusse, Y., T. Maesaka, K. Kieda, and K. Iwanami, 2019: Polarimetric radar observation of the melting layer in a winter precipitation system associated with a south-coast cyclone in Japan. *J. Met. Soc. Japan*, 97, 375-385.

Extending Forecast Range and Introducing an Ocean Mixed Layer Model in JMA's Mesoscale NWP System

SAWADA Masahiro, KITAMURA Yuji, MATSUBAYASHI Kengo, KUSABIRAKI Hiroshi,
NISHIMOTO Shusuke, AIKAWA Takuya, YAMASAKI Yukihiro

Japan Meteorological Agency

(email: msawada@met.kishou.go.jp)

1. Introduction

JMA operates a meso-scale model (MSM) to provide information for disaster prevention and aviation safety (JMA 2019). The model's physics parameterization was upgraded and the number of vertical layers was increased in March 2022, and an extension of the forecast range is planned for June 2022. This report provides summarizes the upgrade (MSM2203) from the previous system (MSM2003) with focus on sea surface processes for improved typhoon intensity forecasting.

2. Model updates

The number of vertical levels in MSM2203 is increased from 76 to 96 and the topmost level from 21.8 to 37.5 km to incorporate satellite data sensitive to temperature in the upper troposphere in meso-scale analysis.

The MSM forecast range is extended from 51 to 78 hours at 00 and 12 UTC to provide prefectural-scale precipitation information up to three days ahead, especially for potentially disastrous typhoons and heavy rainfall.

In MSM2003, mixing-length scale formulation for the planetary boundary layer scheme was modified based on Olson et al. (2019) to reduce excessive turbulent transport caused by turbulent kinetic energy in the free atmosphere. For the land surface scheme, evapotranspiration processes were also revised to represent a better diurnal cycle of surface temperature and moisture. A one-dimensional ocean mixed layer (OML) model based on Price et al. (1986) was additionally introduced to alleviate typhoon over-intensification, which relates to the use of a fixed SST as a boundary condition of the MSM so that the sea surface cooling induced by typhoons is not represented. The OML model represents ocean vertical mixing relating to static stability, mixed layer stability, shear flow stability associated with air-sea heat flux and wind stress. The vertical grid spacing of the OML is 5 m and the bottom depth is set as 100 m to save computational time. The initial sea surface temperature (SST) is determined from high-resolution merged satellite and in-situ SST data provided by JMA. The initial conditions for water temperature and salinity are obtained from World Ocean Atlas 2018 monthly mean climatology data (Locarnini et al. 2018, Zweng et al. 2018). Nudging is implemented in the OML model to avoid SST drift from a realistic state. The e-folding time for nudging is a function of distance from land and seafloor depth with a maximum of one day over open ocean.

3. Case study: Typhoon Krosa (2019)

Figure 1 exemplifies the effects of the OML model on SSTs and mean sea-level pressure for Typhoon Krosa (2019) with a lead time of 72 hours for MSM2003 and MSM2203. The latter shows sea surface cooling along the typhoon track, which was roughly consistent with SST analysis (not shown). The central pressure values were 949.3 hPa in MSM2003, 965.4 hPa in MSM2203 and 970 hPa in best-track analysis. MSM2203 significantly alleviated typhoon over-intensification, mainly due to typhoon-induced sea-surface cooling through OML and reduced latent heat flux due to sea salinity effect.

4. Verification

Figure 2 shows a statistical evaluation of mean errors and root-mean-square errors (RMSEs) of central sea-level pressure for MSM2003 and MSM2203 with regards to best track from 1 July to 15 September 2020 (summer). The negative bias and RMSE are significantly reduced in MSM2203 as compared with MSM2003, and there is little difference in typhoon track forecast errors between the two (not shown). The bias score is lower for the whole forecast range in MSM2203, and the equitable threat score (ETS) is also slightly higher for the forecast range between 30 to 78 h in MSM2203.
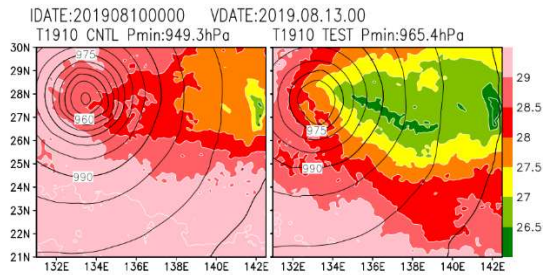

Figure 1: Horizontal pattern of mean sea-level pressure (contours: 5-hPa intervals) and SST (shading: degrees Celsius) for Typhoon Krosa (2019) with MSM2003 (left) and MSM2203 (right). Forecasts initialized at 00 UTC on 10 October 2019.
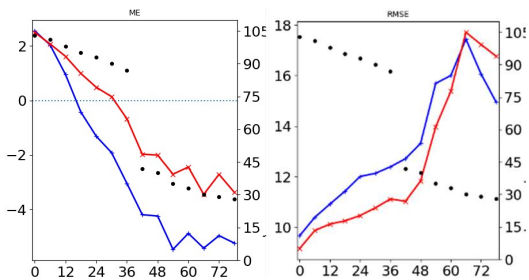

Figure 2: Time-series of mean errors (left) and RMSE (right) for central pressure (hPa) in summer with MSM2003 (blue) and MSM2203 (red). Dots represent the number of samples at each forecast lead time (right axis).
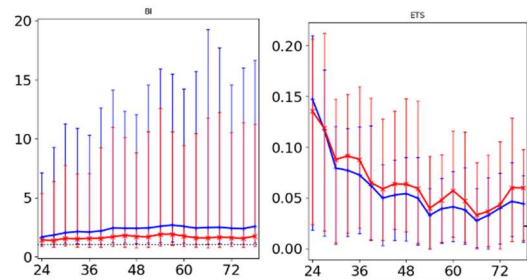

Figure 3: Bias score (left) and ETS (right) for 24-h cumulative precipitation forecasts at a 200 mm threshold for summer. Verification grid size: 20 km; blue: MSM2003; red: MSM2203.

Reference

JMA, 2019: Outline of Operational Numerical Weather Prediction at JMA. Japan Meteorological Agency, Tokyo, Japan.

Locarnini, R. A., A. V. Mishonov, O. K. Baranova, T. P. Boyer, M. M. Zweng, H. E. Garcia, J. R. Reagan, D. Seidov, K. Weathers, C. R. Paver, and I. Smolyar, 2018. World Ocean Atlas 2018, Volume 1: Temperature. A. Mishonov Technical Ed.; NOAA Atlas NESDIS 81, 52pp.

Olson, J. B., J. S. Kenyon, W. A. Angevine, J. M. Brown, M. Pagowski, and K. Sušelj, 2019: A description of the MYNN-EDMF scheme and the coupling to other components in WRF-ARW. NOAA Tech. Memo. OARGSD, 61, 37 pp.

Price, J. F., R. A. Weller, and R. Pinkel, 1986: Diurnal cycling: Observations and models of the upper ocean response to diurnal heating, cooling, and wind mixing. J. Geophys. Res., 91, 8411–8427.

Zweng, M. M., J. R. Reagan, D. Seidov, T. P. Boyer, R. A. Locarnini, H. E. Garcia, A. V. Mishonov, O. K. Baranova, K. Weathers, C. R. Paver, and I. Smolyar, 2018. World Ocean Atlas 2018, Volume 2: Salinity. A. Mishonov Technical Ed.; NOAA Atlas NESDIS 82, 50pp.

Atmospheric River Analysis and Forecast System (AR-AFS): Atmospheric River Reconnaissance 2021 Dropsonde Data Impact Study on California Precipitation Forecasts

Keqin Wu[1], Xingren Wu[2], Vijay Tallapragada[3],and F. Martin Ralph[4]

1 NGI at EMC/NCEP/NWS/NOAA, College, Park MD 20740
2 IMSG at EMC/NCEP/NWS/NOAA, College Park MD 20740
3 EMC/NCEP/NWS/NOAA, College Park, MD 20740
4 CW3E, Scripps Institution of Oceanography, UC San Diego, CA 92093

Email: Keqin.Wu@noaa.gov

1. Introduction

Atmospheric rivers (ARs) are narrow corridors of concentrated atmospheric moisture which are responsible for the majority of extreme rainfall over western North America. G. Wick, et al. [1] showed that numerical weather prediction (NWP) models can have large forecast errors in predicting ARs. AR Reconnaissance (ARR) campaigns plan and deploy aircraft over the northeast Pacific to collect observations to support improved AR forecasts. This paper describes the application of the Atmospheric River Analysis and Forecast System (AR-AFS), a stand-alone high-resolution regional model, to study AR 2021 dropsonde data impact on the forecast of AR-related precipitation in California.

2. AR-AFS Model

AR-AFS is based on the FV3 dynamical core and uses initial and boundary conditions from the NCEP operational Global Forecast System version 16 (GFSv16). The AR-AFS model has 64 vertical layers and a fine horizontal resolution of 3 km over the Northeast Pacific and Western North America, and provides 5 day forecasts. The physics parameterizations include the GFS land surface scheme, Thompson microphysics scheme, and hybrid eddy-diffusivity mass-flux (EDMF) PBL scheme. Figure 1 shows the model domain, a forecasted AR landing on California, and the AR-introduced heavy precipitation.
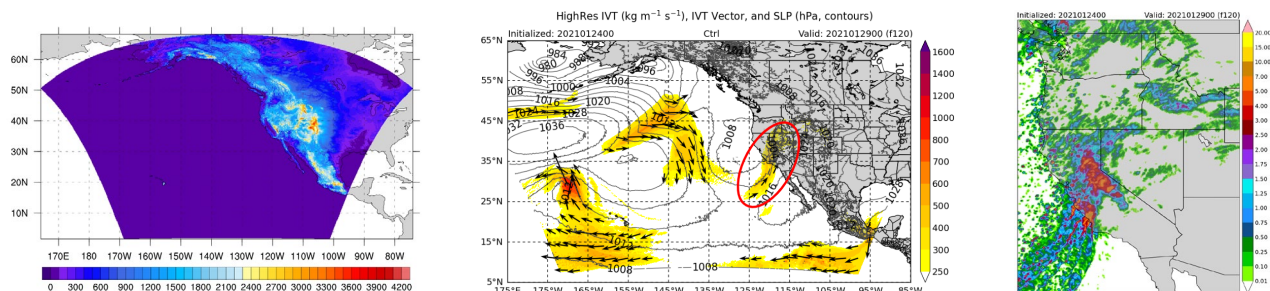

Figure 1 AR-AFS AR forecast (initialized on 00Z Jan 24, 2021 and valid on 00Z Jan 29, 2021). Left: AR-AFS domain; Middle: IVT (Integrated Water Vapor Transport) and an AR (the orange band inside the red circle); Right: 24-hour precipitation on West Coast.

3. Data Experiments

We examine the impact of the AR supplemental observation dropsonde data on the forecast of an AR in California on January 23-29, 2021. It was a scale 2 AR event that impacted Central California with heavy rainfall. Six consecutive intensive observation periods (IOPs) were executed by flights sampling the same synoptic system from January 23 to 28, 2021. GFSv16 control (Ctrl) and denial experiments (Deny) were conducted by using or denying the dropsonde data in the Data Assimilation of the model. AR-AFS model uses GFSv16 Ctrl and Deny outputs as the initial and boundary conditions for its Ctrl and Deny runs.

A series of analyses were conducted to compare Ctrl and Deny in high precipitation regions for individual IOPs or consecutive IOPs. Ctrl gives overall better precipitation forecasts in terms of magnitudes and locations. Sample analysis results are shown in Figures 2-3. Among the average precipitation from Ctrl, Deny, and observation (Stage IV), 4 out of 5 IOPs have a positive impact on precipitation in both selected regions (Fig. 2). In Figure 3a, the same

two objects (precipitation >=2 inches) matched with the observed are found in both Ctrl and Deny, but Ctrl has a higher average rate (0.97) than Deny (0.93). This indicates a higher overall similarity (closer locations, a bigger overlap, etc.) between the Ctrl and observations. For a threshold of 2.5 inches (Fig. 3b), all 4 observed objects match the 4 objects in Ctrl but only 3 matched objects are found in Deny.
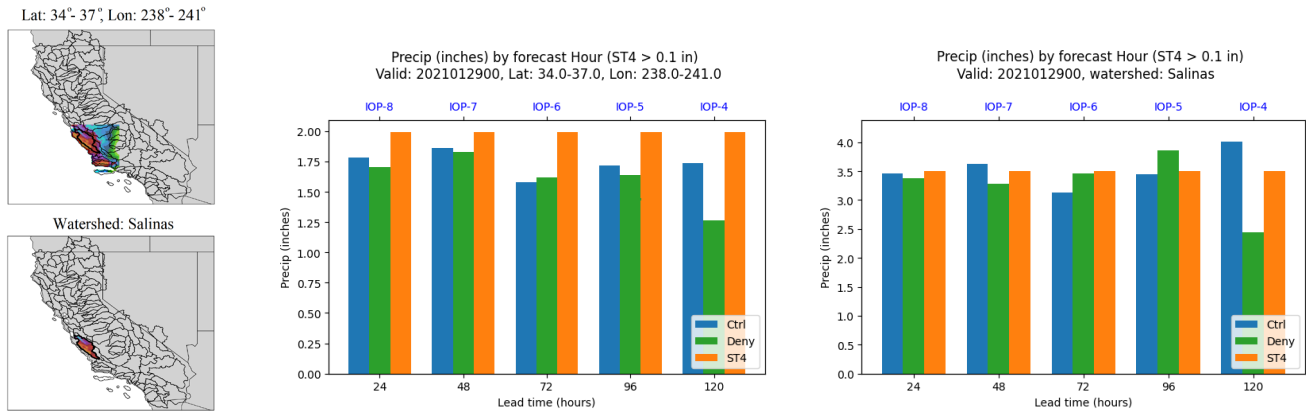

Figure 2 Region average of 24-hour precipitation of AR-AFS Ctrl, AR-AFS Deny, and Stage IV (observation). Forecasts are initialized on 00Z Jan 24, 2021, and valid on 00Z Jan 29, 2021. Left: a high precipitation region and a watershed. Middle and Right: the average precipitation with a cut-off of 0.1 inch over the region and the watershed.
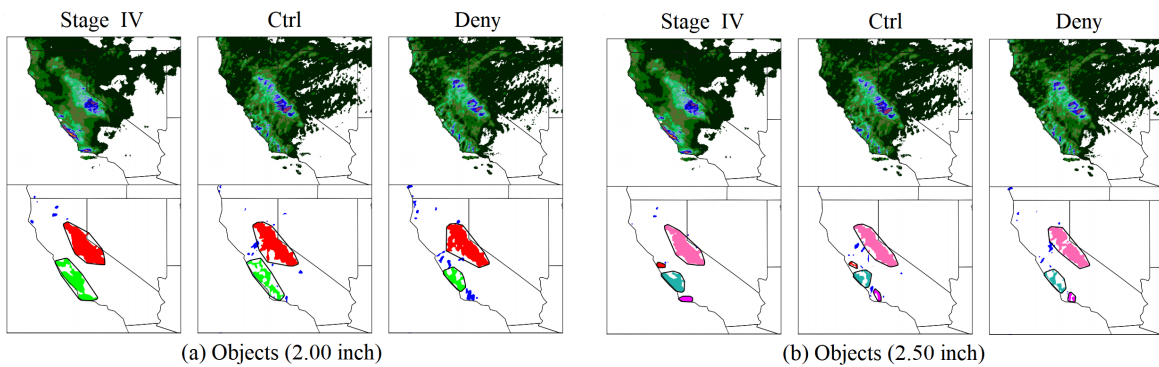

Figure 3 Mode Verification [2] of 24-hour precipitation of AR-AFS Ctrl, AR-AFS Deny, and Stage IV (observation). Forecasts are initialized on 00Z Jan 28, 2021, and valid on 00Z Jan 29, 2021. (a) Objects defined as precipitation >=2 inches. (b) Objects defined as precipitation >=2.5 inches.

4. Summary

AR-AFS is developed and applied to the data impact study of ARR. Positive impacts on the AR-AFS forecast skill using dropsondes data are found from consecutive IOPs in January 2021 for California. The study also supplements the concurrent GFS Ctrl and Deny experiments as AR-AFS uses GFS as its initial fields. In addition, the high resolution of AR-AFS helps with the study of data impact on small regions of interest.

References

[1] Wick, G. A., Neiman, P. J., Ralph, F. M., & Hamill, T. M. (2013). Evaluation of Forecasts of the Water Vapor Signature of Atmospheric Rivers in Operational Numerical Weather Prediction Models, *Weather and Forecasting*, *28*(6), 1337-1352.

[2] Davis, C.A., Brown, B., & Bullock, R. (2006). Object-Based Verification of Precipitation Forecasts. Part II: Application to Convective Rain Systems. *Monthly Weather Review, 134*, 1785-1795.

Three-Dimensional Real-Time Mesoscale Analysis (3D-RTMA) Quality Assessment for Aviation Applications

Gang Zhao[1], Manuel Pondeca[1], Matthew Morris[2], Edward Colon[1],
Ricardo Todling[3], and Jacob Carley[4]
[1]IMSG at NOAA/NWS/NCEP/EMC; [2]SRG at NOAA/NWS/NCEP/EMC;
[3]NASA/GSFC/GMAO; [4]NOAA/NWS/NCEP/EMC
Email Address: Gang.Zhao@noaa.gov

To alleviate the impact of missing METAR observations on aircraft operations (e.g., delays or cancellations), the Environmental Modeling Center (EMC) began providing pseudo-observations of 2-m temperature, derived from the operational Real-Time Mesoscale Analysis (RTMA), at select airport sites in July 2015. The overarching goal of this work is to inform the Federal Aviation Administration (FAA) of whether the RTMA could be used as a substitute for additional weather elements (e.g., wind speed, ceiling). In the first phase of this work, data denial experiments were used to perform a quality assessment of the RTMA (Morris et al. 2020). In the second phase, a real-time quality monitoring system was developed at EMC for the future 3D-RTMA system. Due to the high computational cost of data denial experiments, an adjoint-based observation impact computation approach was adopted in this work (e.g., Baker 2000; Baker and Daley 2000; Zhu and Gelaro 2008; Tyndall and Horel 2013; Todling 2013). This system can be used to ascertain the 3D-RTMA analysis quality when a METAR observation is missing and help inform decisions about whether interpolated 3D-RTMA products would be a reliable substitute for missing METAR observations.

Using the adjoint-based observation impact code in the Gridpoint Statistical Interpolation (GSI) system, which is used as the analysis scheme for 3D-RTMA, the quality monitoring system was successfully integrated into the workflow of the experimental 3D-RTMA system. This system was run every 3 hours over a 2-month period, from 00Z on 1 October 2021 to 21Z on 30 November 2021, and provided the observation sensitivity, innovation, impacts, and impact-related derivatives (e.g., the fractional impact) of METAR observations at select airports simultaneously for each analysis cycle in real-time. Figure 1 shows an example of the impact analysis results for the temperature reports at and around the METAR site KDFW (Dallas/Fort Worth International Airport). One sees that the absolute value of the relative impact of KDFW is comparable to that at several nearby observations, which suggests that it would be feasible to replace a missing KDFW report with the RTMA analysis. As expected, the relative impacts around KDFW are significantly smaller than in areas of sparse observation density, such as around KBIL (Billings-Logan International Airport in Montana; not shown).

A long-term time series of the results (e.g., sensitivity, impact, fractional impact, etc.) can be generated for any METAR station of interest by continuously running this system and be used to quantify the impact of missing observations. Approximate analytical and graphical-derived relationships between the observation impact (and fractional impact) of a given METAR observation and the expected change to the local analysis increment should the METAR be absent from the assimilation were investigated for various observation types (e.g., 2-m temperature and moisture). Current results show that this adjoint-based quality monitoring system for 3D-RTMA is very promising. It is expected that with additional tuning over a longer run period, the system will be able to provide reliable information to the FAA regarding the feasibility of using the analysis products in lieu of missing METAR reports.
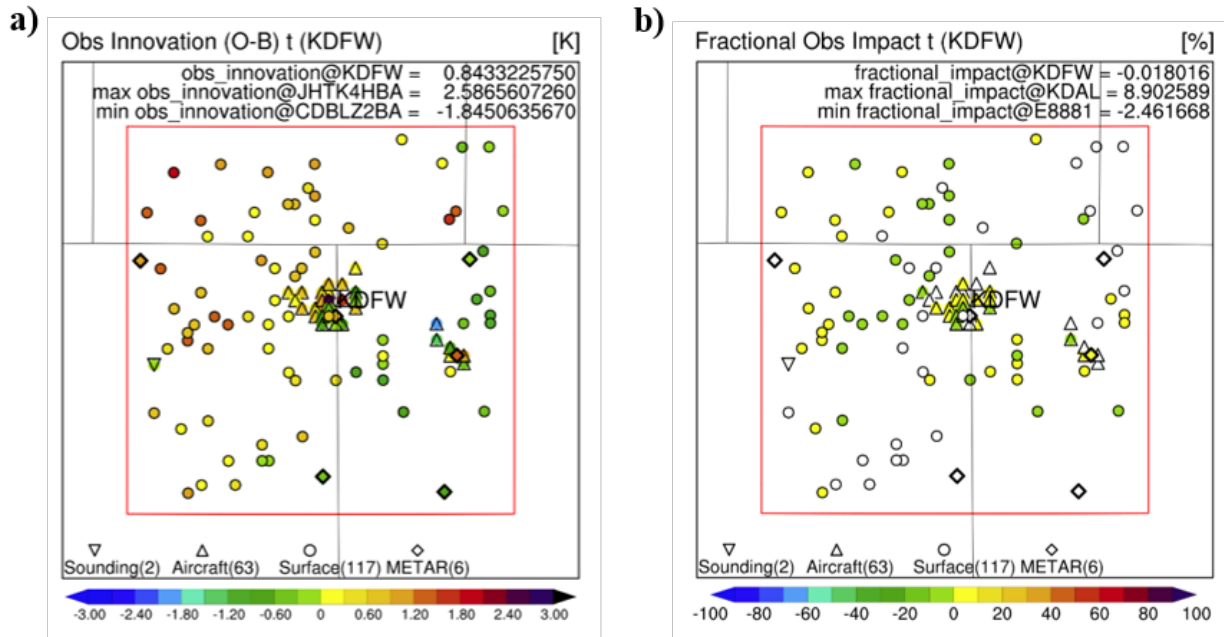
Figure 1 Observation a) innovations and b) fractional impacts for temperature observations around KDFW (Dallas/Fort Worth International Airport) for the 00Z cycle on 11 October 2021. Hollow markers represent observations that contribute negligible values to the specific quantity being displayed.

References

Baker, N., 2000: Observation adjoint sensitivity and the adaptive observation-targeting problem. Ph.D. thesis, Naval Postgraduate School, Monterey, CA, 332 pp.

Baker, N. L., and R. Daley, 2000: Observation and background adjoint sensitivity in the adaptive observation-targeting problem. *Quart. J. Roy. Meteor. Soc.*, **126**, 1431-1454.

De Pondeca, M. S. F. V., and Coauthors, 2011: The real-time mesoscale analysis at NOAA's National Centers for Environmental Prediction: Current status and development. *Wea. Forecasting*, **26**, 593-612, https://doi.org/10.1175/WAF-D-10-05037.1

Morris, M. T., J. R. Carley, E. Colón, A. Gibbs, M. S. F. V. De Pondeca, and S. Levine, 2020: A quality assessment of the Real-Time Mesoscale Analysis (RTMA) for aviation. *Wea. Forecasting*, **35**, 977–996, https://doi.org/10.1175/WAF-D-19-0201.1

Todling, R., 2013: Comparing two approaches for assessing observation impact. *Mon. Wea. Rev.*, **141**, 1484-1505, https://doi.org/10.1175/MWR-D-12-00100.1

Tyndall, D. P., and J. D. Horel, 2013: Impacts of mesonet observations on meteorological surface analyses. *Wea. Forecasting*, **28**, 254–269, https://doi.org/10.1175/WAF-D-12-00027.1.

Zhu, Y., and R. Gelaro, 2008: Observation sensitivity calculations using the adjoint of the Gridpoint Statistical Interpolation (GSI) analysis system. *Mon. Wea. Rev.*, **136**, 335-351.